

SOFIA observations of 30 Doradus: I - Far-Infrared dust polarization and implications for grain alignment and disruption by radiative torques

LE NGOC TRAM,^{1,*} THIEM HOANG,^{2,3} ENRIQUE LOPEZ-RODRIGUEZ,⁴ SIMON COUDÉ,¹ ARCHANA SOAM,¹ B-G ANDERSSON,¹ MIN-YOUNG LEE,² LARS BONNE,¹ WILLIAM D. VACCA,¹ AND HYESEUNG LEE²

¹*Stratospheric Observatory for Infrared Astronomy, Universities Space Research Association, NASA Ames Research Center, MS 232-11, Moffett Field, 94035 CA, USA*

²*Korea Astronomy and Space Science Institute, Daejeon 34055, South Korea*

³*Korea University of Science and Technology, 217 Gajeong-ro, Yuseong-gu, Daejeon, 34113, South Korea*

⁴*Kavli Institute for Particle Astrophysics and Cosmology (KIPAC), Stanford University, Stanford, CA 94305, USA*

(Accepted 2021)

ABSTRACT

Located in the Large Magellanic cloud and mostly irradiated by a massive-star cluster R 136, 30 Doradus is an ideal target to test the leading theory of the grain alignment and rotational disruption by Radiative Torques (RATs). Here, we use publicly available polarized thermal dust emission observations of 30 Doradus at 89, 154, and 214 μm using SOFIA/HAWC+. We analyse the variation of the dust polarization degree (p) with the total emission intensity (I), the dust temperature (T_{d}), and the gas column density (N_{H}) constructed from *Herschel* data. The 30 Doradus complex is divided into two main regions relative to R 136, namely North and South. In the North, we find that the polarization degree first decreases and then increases before decreasing again when the dust temperature increases toward the irradiating cluster R 136. The first depolarization likely arises from the decrease of grain alignment efficiency toward the dense medium due to the attenuation of the interstellar radiation field and the increase of the gas density. The second trend (the increase of p with T_{d}) is consistent with the RAT alignment theory. The final trend (the decrease of p with T_{d}) is consistent with the RAT alignment theory only when the grain rotational disruption by RATs is taken into account. In the South, we find that the polarization degree is nearly independent of the dust temperature, while the grain alignment efficiency is higher around the peak of the gas column density and decreases toward the radiation source. The latter feature is also consistent with the prediction of the rotational disruption by RATs.

Keywords: ISM: dust, extinction – ISM: clouds – ISM: individual objects (30 Doradus, LMC) – ISM: polarization

1. INTRODUCTION

Grain alignment induces the polarization of background starlight as well as the polarization of thermal dust emission. Dust polarization induced by aligned dust grains is widely used to map magnetic fields (see e.g., Lazarian 2007). A leading theory describing grain alignment is based on Radiative Torques (hereafter RATs), which arises from the interaction of an anisotropic radiation field with irregular dust grains Dolginov & Mytrophanov 1976; Draine & Weingartner 1996; Lazarian & Hoang 2007; see Lazarian et al. 2015 and Andersson et al. 2015 for recent reviews). According to the RAT alignment theory, the alignment efficiency of dust grains depends on the radiation field and the local gas properties (e.g., Hoang et al. 2021; Soam et al. 2021a). Gas collisions tend to damp the grain rotation and randomize the grain orientation, whereas RATs act to spin-up and align dust grains. Therefore, toward the center of

Corresponding author: Le Ngoc Tram
 nle@mpifr-bonn.mpg.de

* Current address: Max-Planck-Institut für Radioastronomie, Auf dem Hügel 69, 53-121, Bonn, Germany

a dense cloud, the degree of grain alignment by RATs decreases due to the attenuation of the interstellar radiation field (ISRF) and the increase of gas density. This results in the decrease of the dust polarization degree (p) toward the center of molecular clouds (MCs), i.e., higher gas column density N_{H} (see e.g., Hoang et al. 2021). Numerous observations toward MCs report the decrease of the polarization degree with N_{H} , which favors the RAT alignment theory (Whittet et al. 2008; Alves et al. 2014; Vaillancourt et al. 2020). Note that the tangling of magnetic fields is also suggested to produce the decrease of the polarization with increasing N_{H} (e.g., Jones et al. 1992).

With the advance of high resolution polarimetric facilities (JCMT/POL2, ALMA, SOFIA/HAWC+), one can now observe the polarization induced by dust grains in proximity of an embedded source (e.g., a protostar) where the effect of stellar radiation becomes dominant over that of the ISRF. As a result, toward the embedded source, the RAT alignment theory predicts the increase of the dust polarization with increasing the radiation emission intensity (or dust temperature T_{d} , Hoang et al. 2021). Numerical modeling (Lee et al. 2020) and numerical simulations (Reissl et al. 2016) of dust polarization using the RAT alignment theory report a monotonic increase of the polarization degree of thermal dust emission with increasing the radiation intensity (or T_{d}). Such a correlation of p with T_{d} is an important feature predicted by the RAT alignment theory. As a result, observing dust polarization around a strong radiation source is crucial to test the RAT alignment theory (see e.g., Medan & Andersson 2019; Soam et al. 2021b).

Interestingly, polarimetric observations reveal that the degree of thermal dust polarization does not always increase with the radiation intensity (or dust temperature, T_{d}) and decrease with increasing N_{H} , as implied by the RAT alignment theory. For example, *Planck* observations at 850 μm toward four molecular clouds, including Aquila Rift, Cham-Musca, Orion, and Ophiuchus in the Gould Belt cloud, showed that the polarization degree decreases for $T_{\text{d}} > 19$ K (see Planck Collaboration et al. 2020). Shorter wavelength polarimetric measurements at 500 μm from the air-balloon BLASTPol toward the Vela C also show a similar decrease at $T_{\text{d}} \geq 19$ K (see Fissel et al. 2016). Further shorter wavelength observations by the High-resolution Airborne Wide band Camera Plus (HAWC+) instrument (Harper et al. 2018) aboard the Stratospheric Observatory for Infrared Astronomy (SOFIA) toward the molecular cloud Ophiuchus A at 89 and 154 μm also reported the decrease of the polarization degree for $T_{\text{d}} \geq 25 - 32$ K and $N_{\text{H}} \leq 10^{22} \text{ cm}^{-2}$ (see Santos et al. 2019 and Tram et al. 2021a). For the case of ρ Ophiuchus A, the peak of the dust temperature is close to the central source (a B-type star), while the gas column density peaks further away. Thus, the decrease of the dust polarization degree toward high dust temperatures and low gas column density (toward the source) could not be explained by the loss of grain alignment due to weak radiation intensity or enhanced collisional randomization as in the case of starless cores (Whittet et al. 2008; Alves et al. 2014).

Hoang et al. (2019) realized that large grains cannot survive once being exposed to a strong radiation field owing to the Radiative Torque Disruption (RATD) mechanism (see Hoang 2020 for a review). The RATD mechanism causes the fragmentation of large grains into many smaller species when the centrifugal stress induced by suprathermal rotation due to RATs exceeds the tensile strength of the grain material, which is determined by the binding energy that hold their constituents together. RATD is more efficient for large grains because the RAT efficiency increases with the grain size (Lazarian & Hoang 2007; Hoang & Lazarian 2008). The depletion of large grains due to RATD is expected to result in the decrease of the polarization degree of the thermal dust emission because large grains dominate the polarized emission at long wavelengths.

The first numerical modeling of dust polarization that considers both grain alignment and rotational disruption by RATs was performed in Lee et al. (2020). They found that the dust polarization degree increases monotonically with T_{d} when grains are aligned by RATs and the RATD effect is not taken into account. In the presence of RATD, the polarization degree first increases and then decreases when the dust temperature becomes sufficiently large (i.e., the corresponding radiation strong enough) to activate the RATD effect. The critical temperature for the RATD effect depends on the local gas density and grain tensile strength that depends on the grain structure. Their modeling results could successfully reproduce the anti-correlation $p - T_{\text{d}}$ trend at 850 μm observed by *Planck* (Planck Collaboration et al. 2020). As a result, the variation of p with T_{d} observed toward an intense radiation source becomes an important test for the RAT alignment and RATD theory. The first detailed analysis of the $p - T_{\text{d}}$ relation is carried out in Tram et al. (2021a) for the SOFIA/HAWC+ observations from Ophiuchus A cloud at 89 and 154 μm . The authors found the anti-correlation of $p - T_{\text{d}}$ for sufficiently large T_{d} and show that it could be reproduced by the RAT alignment and RATD. Ngoc et al. (2021) also found the anti-correlation of $p - T_{\text{d}}$ toward the proximity of the LkH α 101 star in the Auriga-California cloud. These studies reveal the importance of RATD that needs to be taken into account together with RAT alignment to interpret dust polarization data observed toward an intense radiation source. Moreover,

observational data also allow us to constrain the physical properties and characteristics of dust grains, such as shape, internal structure, mineralogy, helicity and size distribution.

In this paper, we will use the thermal dust polarization observed by SOFIA/HAWC+ at 89, 154, and 214 μm toward a massive star-forming cloud, 30 Doradus (hereafter 30 Dor), to test the RAT alignment and RATD mechanisms. 30 Dor is located in the Large Magellanic Cloud (LMC) with the distance of ~ 50 kpc from us (e.g., De Marchi et al. 2011) and powered by a massive star cluster R136, with mass of $\simeq 5 \times 10^4 M_\odot$ (see Indebetouw et al. 2009 and references therein) and the bolometric luminosity of $7.8 \times 10^7 L_\odot$ (see Lopez et al. 2011 and references therein). Note that LMC is a low-metallicity galaxy ($Z \simeq 0.5 Z_\odot$, Dufour et al. 1982; Galliano et al. 2008b; Chevance et al. 2016), with a low dust-to-gas ratio (e.g., $\sim 2.5 \times 10^{-3}$, see Roman-Duval et al. 2014; Chevance et al. 2016), which makes the dust-shielding relatively low such that dust grains can be affected by the radiation field over a large scale (see Figure 1). Thus, the 30 Dor cloud offers a valuable environment to test the physics of grain alignment and disruption by RATs. Toward this end, we will concentrate on the correlation of the polarization degree with the emission intensity, the dust temperature, and the gas column density.

This paper is structured as follows. We first present the FIR polarimetric observations of 30 Dor observed by SOFIA/HAWC+ in Section 2. We then present (1) the distribution of the polarization angle and the polarization degree, (2) the relation of the polarization degree with the total intensity, the gas column density, and with dust temperature in Section 3. The implications of the observational data for grain alignment and rotational disruption by RATs are presented in Section 4. The summary of our main findings is presented in Section 5.

2. OBSERVATIONS OF 30 DORADUS

2.1. SOFIA/HAWC+ multi-wavelength polarization

Polarization of thermal dust emission from 30 Dor was observed by SOFIA/HAWC+ at three bands: C at 89 μm , D at 154 μm , and E at 214 μm . The beams sizes (Full-Width-at-Half-Maximum, FWHM) are 7.8'', 13.6'', and 18.2'' at 89 μm , 154 μm , and 214 μm , respectively. Data are publicly available under the Strategic Director's Discretionary Time (S-DDT) program (PI: Yorke, H., ID: 76_0001), which observations were taken during the SOFIA New Zealand deployment in July 2018. Data have been presented by Gordon et al. 2018 and no further data reduction has been performed.

For the linear polarization, the polarized intensity is defined as (Gordon et al. 2018)

$$I_p = \sqrt{Q^2 + U^2} \quad (1)$$

with Q the Stokes parameter Q, U the Stokes parameter U. The associated error is then

$$\sigma_{I_p} = \left[\frac{(Q\sigma_Q)^2 + (U\sigma_U)^2}{Q^2 + U^2} \right]^{1/2} \quad (2)$$

with σ_Q the error of Stokes Q, and σ_U the error of Stokes U.

The debiased polarization degree is calculated as

$$p = \frac{100}{I} \sqrt{Q^2 + U^2 - \sigma_{I_p}^2} = 100 \frac{I_p}{I} \quad (\%) \quad (3)$$

with I the Stokes I parameter. The associated error is then

$$\sigma_p = p \left[\left(\frac{\sigma_{I_p}}{I_p} \right)^2 + \left(\frac{\sigma_I}{I} \right)^2 \right]^{1/2} \quad (4)$$

with σ_I the error of Stokes I.

Finally, the polarization angle and its error are given by

$$\theta = \frac{1}{2} \arctan \left(\frac{U}{Q} \right) \quad (5)$$

and

$$\sigma_\theta = \frac{1}{2} \frac{\sqrt{(Q\sigma_Q)^2 + (U\sigma_U)^2}}{Q^2 + U^2}. \quad (6)$$

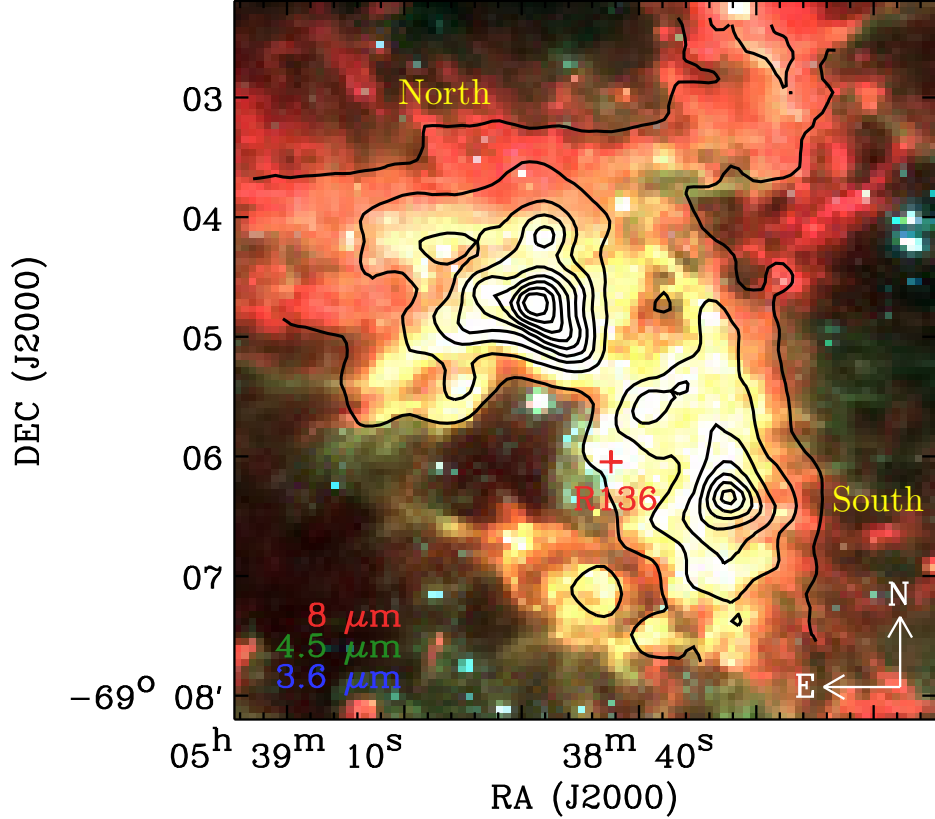


Figure 1. Background is a RGB composite image with R: $8\text{ }\mu\text{m}$, G: $4.5\text{ }\mu\text{m}$, and B: $3.6\text{ }\mu\text{m}$. The black contours show an example of the FIR observations at $154\text{ }\mu\text{m}$ with SOFIA/HAWC+. There are two main regions in 30 Dor: North and South in relative to the massive star cluster, R136. The data analyzed in this work locate in the strong radiation field.

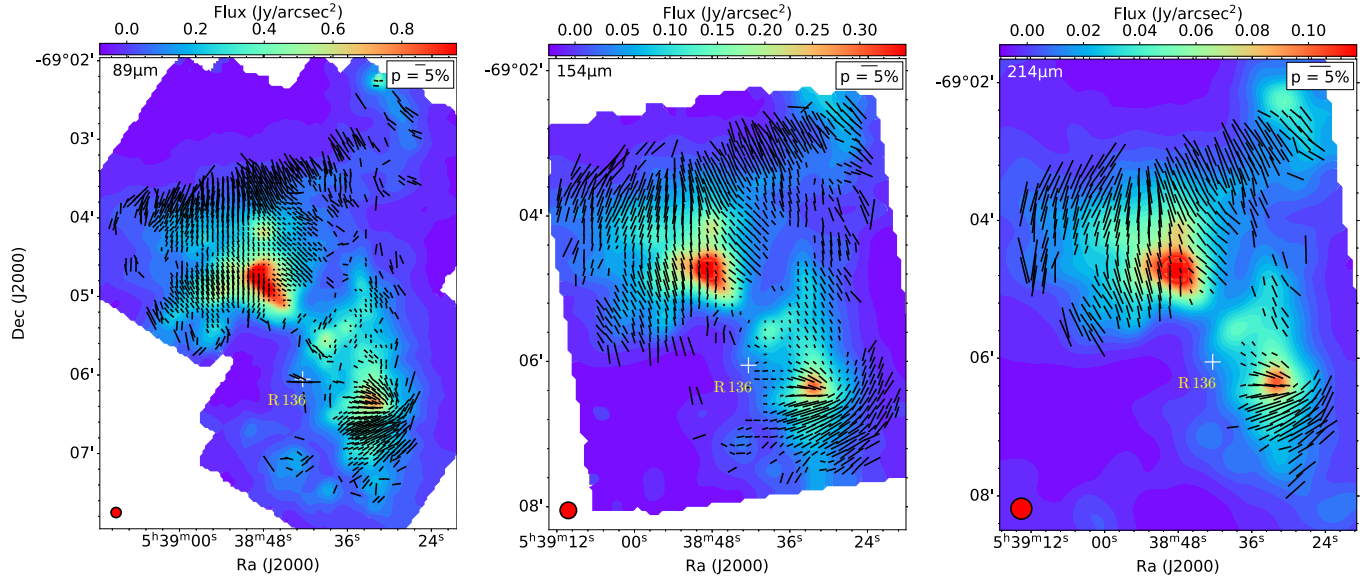


Figure 2. Polarization maps (E-vectors) of 30 Dor observed using SOFIA/HAWC+ at $89\text{ }\mu\text{m}$ (left), $154\text{ }\mu\text{m}$ (middle), and $214\text{ }\mu\text{m}$ (right). The background color is the total intensity (Stokes I). The vectors are selected within the thresholds of $I/\sigma_I \geq 100$ and $p/\sigma_p \geq 3$ (see Section 2.1). The beam size (red circle) at the respective wavelengths and a 5% polarization measurement (top-right) are shown. The location of R136 (white cross) is shown in every panel.

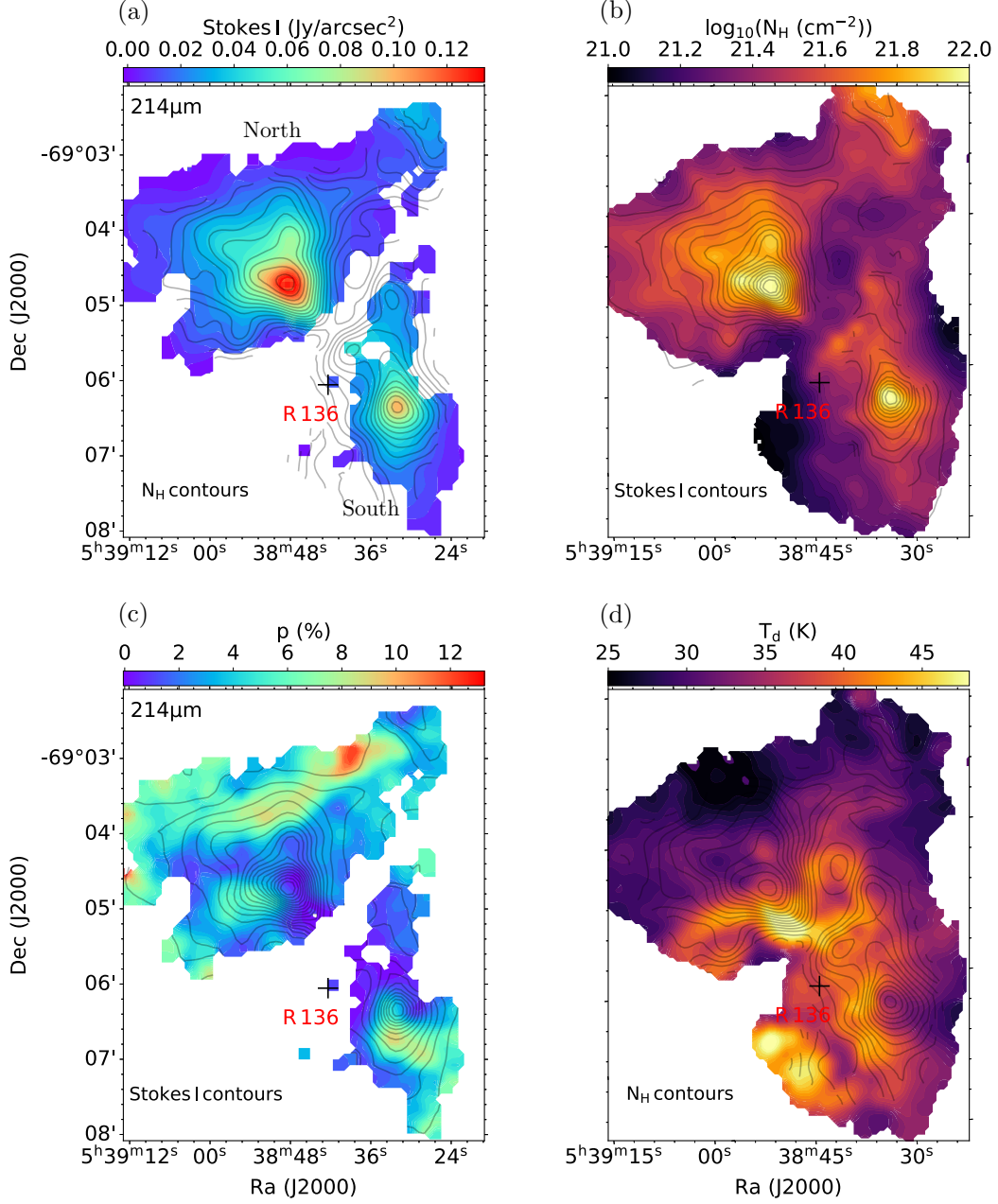


Figure 3. Panels(a,c): Maps of the total intensity and the polarization degree at $214\mu\text{m}$ after masking from the common sky positions in which all 3 bands in Figure 2 detected the signal. Panels(b,d): Maps of the gas column density and the dust temperature. The black cross locates the massive star cluster R136. The total intensity correlates well to the gas column density. The gas column density peak is offset from the dust temperature, whose peak is close to R136.

We then performed quality cuts to obtain statistically significant polarization measurements. The quality cuts on the polarization map are very conservative. In this work, we mask our HAWC+ maps by using two common thresholds. The first quality cut depends on the signal-to-noise ratio of the Stokes-I (I/σ_I), we adopt $I/\sigma_I \geq 100$, which allows $\sigma_p \simeq \sqrt{2} \times (I/\sigma_I)^{-1} = 1.4\%$ ¹. The second threshold is the signal-to-noise ratio of the fractional polarization $p/\sigma_p \geq 3$. Figure 2 show the final map of the polarization vectors (E-vectors, not B-vectors). The length of the polarization

¹ This approximation is derived from Equation 4 by assuming that $\sigma_Q = \sigma_U$

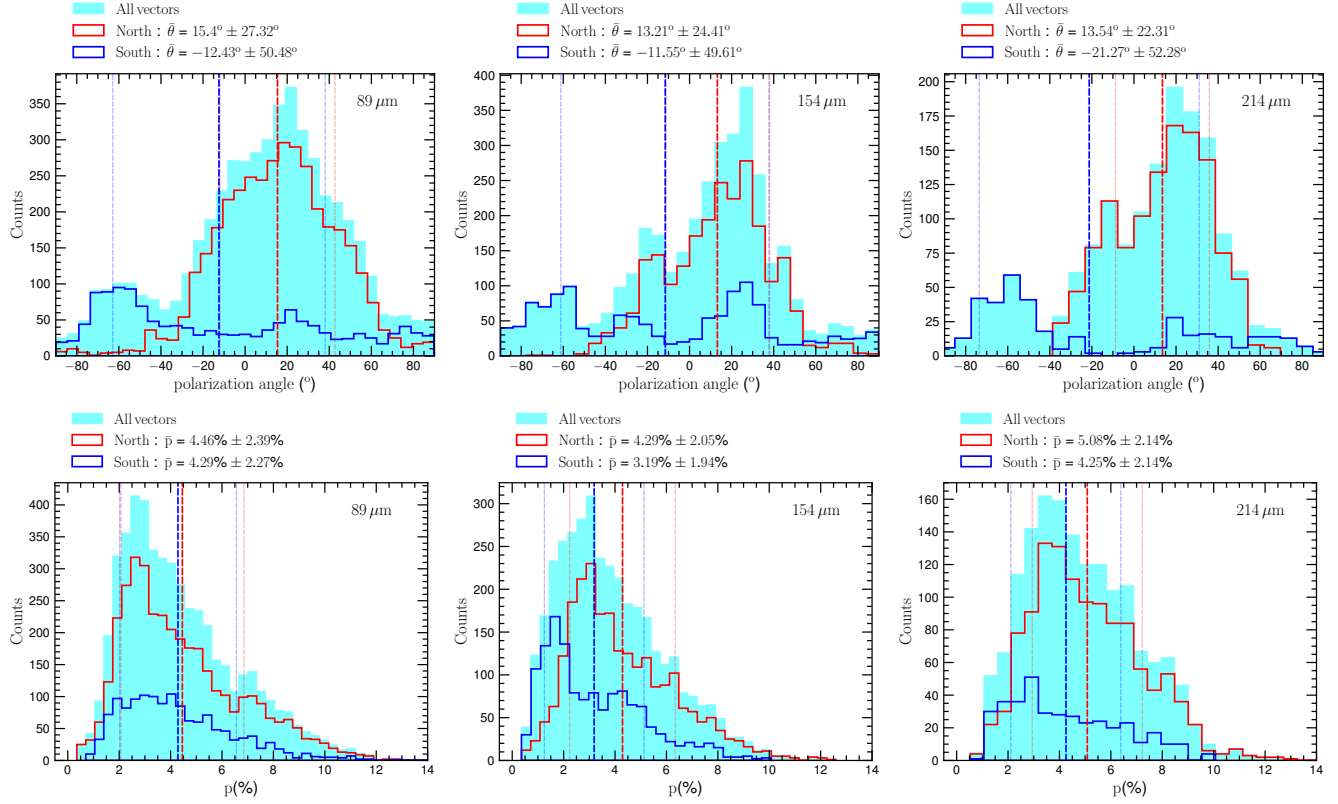


Figure 4. Distribution of the polarization angle (upper panels) and the polarization degree (lower panels) in 3 bands (from left to right). The cyan, red and blue are the distributions of the polarization measurement in the entire region, in the North and in the South regions (see Figure 2), respectively. The vertical dashed red and blue lines are the weighted mean of the North and the South distributions. The corresponding thinner lines represent for the 1σ uncertainties.

measurements is referenced to 5% of polarization degree. Data for band C (89 μm), D (154 μm) and E (214 μm) is shown from left to right, and the background color is the original total intensity (Stokes I). Figure 3(a,c) show the final maps of the Stokes I and the polarization degree at 214 μm as an example. The correlations to the gas column density are visualized by the black contours.

2.2. Gas column density and dust temperature

We constructed the maps of dust temperature, T_d , and the gas column density, $N_{\text{H}} \simeq N(\text{H} + \text{H}_2)$, using *Herschel* data at 100, 160, 250, 350 and 500 μm from HERITAGE (Meixner et al. 2013). The observations were registered and sampled to the 160 μm with a pixelscale of 3'' and FWHM = 11.4'', then a modified black-body function was used to fit to each of the line-of-sight (LOS) SED with an assumed spectral index $\beta = 1.62$. This value was taken as the median from the range of $\beta \sim 1.5 - 1.8$ by Gordon et al. (2014), and $\beta = 2.0$ used by Bernard et al. (2008).

Panels (b,d) in Figure 3 show the maps of the gas column density and dust temperature in 30 Dor. Toward R 136, the dust temperature increases, while the gas column density first increases and then decreases after its peak, which is further away from the center. The correlations are visualized by the black contours in these maps. In addition, the dust temperature (gas column density) in the North is hotter (denser) than in the South.

3. RESULTS

We now show the results analyzing the polarization degree of thermal dust emission in 30 Dor in terms of the total emission intensity, dust temperature and gas column density.

3.1. Variation of polarization in 30 Dor

The upper panels in Figure 4 show the distribution of the polarization angle of the thermal dust polarization in 30 Dor at 3 bands. We chose to use a position angle span of -90 to +90 to center the position angles around the peak of

Bands	$\theta^\circ(\pm 1\sigma)$		$p\%(\pm 1\sigma)$	
	North	South	North	South
89 μm	15.4(27.32)	-12.43(50.48)	4.46(2.39)	4.29(2.27)
154 μm	13.21(24.41)	-11.55(49.61)	4.29(2.05)	3.19(1.94)
214 μm	13.53(22.31)	-21.27(52.28)	5.08(2.14)	4.25(2.14)

Table 1. Mean value and uncertainties of the polarization angle (θ) and the polarization degree (p) in the North and South regions within 3 bands.

the distribution. The variation of the polarization angle is very similar for the three bands. The distributions of all vectors are shown by the cyan area, which shows that the polarization vectors vary quite significantly, spanning from -90° to 90° , and peaks at around 20° and -60° . The first peak is characterized of the polarization in the North (see the red distribution). The second peak originates predominately in the South (see the blue distribution), which has a more random statistic. These distributions have the same bin width, which is chosen following the Freedman-Diaconis rule in python-package² from the all vectors. The weighted-mean values and the uncertainties have been calculated as shown by the dashed vertical thick and corresponding thin lines, whose values are listed in Table 1.

The lower panels in Figure 4 show the distribution of the polarization degree in 3 bands. The distribution peaks at between 2% and 4%. The red and blue histograms show the distributions in the North and South, respectively. The choice of the bin width is the same as above. The weighted mean and the associated 1σ uncertainties are showed by the dashed vertical thick and thin lines, whose values are also listed in Table 1. Notably, the σ is larger than the maximum associated uncertainty of 1.4%, thus the 1σ is intrinsically associated to changes in the source.

3.2. Polarization degree versus total intensity

Figure 5 shows the relation of the polarization degree to the total intensity for all 3 bands in the North region. We first fit the observational data with a single power-law function (solid orange line) using the LMFIT python-package (Newville et al. 2014), and compare it with the limiting case of $\alpha = 1$ (black dashed line). The best fit indicates the slope of $\alpha = 0.6 \pm 0.01$ at $89 \mu\text{m}$ is steeper than 0.5 (in the case the medium is fully turbulent, Jones et al. 1992) and the estimated slopes at $154 \mu\text{m}$ ($\alpha = 0.34 \pm 0.02$) and $214 \mu\text{m}$ ($\alpha = 0.46 \pm 0.02$) are shallower than 0.5. We then fit the data with a double power-law function (solid and dashed blue line) using the piecewise linear least square fit PWLF (Jekel & Venter 2019). The best fits illustrate two distinct slopes, whose transitions are marked by the dashed dotted vertical lines. The transitions occur at $0.28 \pm 0.02 \text{ Jy/arcsec}^2$, $0.05 \pm 0.01 \text{ Jy/arcsec}^2$, and $0.02 \pm 0.003 \text{ Jy/arcsec}^2$ at $89 \mu\text{m}$, $154 \mu\text{m}$, and $214 \mu\text{m}$, respectively. In the latter case, as the intensity increases, the polarization degree first declines rapidly with a steep slope of $\alpha > 0.5$ (solid blue line), and then varies with a shallow slope with $\alpha < 0.5$ (dashed blue line). The first steep slope is still shallower than $\alpha = 1$ predicted by the model in which grains are only aligned in the outer envelope of the cloud (see e.g., Hoang et al. 2021). We note that the slope difference gets smaller for longer wavelengths.

Figure 6 shows the relation of the polarization degree to the total intensity for all 3 bands in the South region (panels a,b,c). The relations are complex, but the data appear to group into two different clusters. We then used the BAYESIANGAUSSIANMIXTURE library in SCIKIT-SKLEARN python-package (Pedregosa et al. 2011) to classify the data points into 2 groups. Since the separation at $89 \mu\text{m}$ is less obvious than at 154 and $214 \mu\text{m}$, the classification works well at these longer wavelengths and fails at $89 \mu\text{m}$. Thus, to make it consistent, we classify this case into 3 groups then merge two of them together. Each cluster is plotted in a different color and is fitted by a power law, as shown in the legend. The polarization degree is higher, and the slope is steeper from one cluster to another.

To better understand the observed features, we show in panels (e) and (d) of Figure 6 the spatial positions of these two clusters at $214 \mu\text{m}$ as an example. The central region (colored area in panel e) seems to be shielded partially from the irradiation of R 136, whereas the outer region (colored area in panel d) contains a near-side region which is directly irradiated by the source R 136. Surprisingly (also differing from the North), the high polarization degree and shallower slope of the $p - I$ diagram is seen for the central region, located around the intensity peak (or the gas column density peak, see Figure 3a). Moreover, the polarization degree in the near-side region (close to R 136) is much lower

² <https://docs.astropy.org/en/latest/visualization/histogram.html>

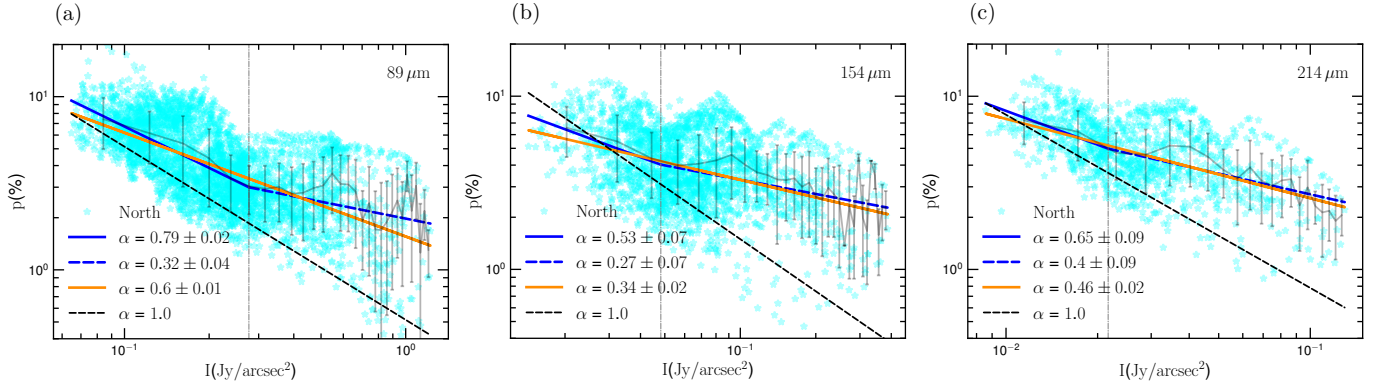


Figure 5. Relation of the polarization degree and the total intensity in 3 bands in the North region. The gray error bars are the mean-weighted within the bins of each data. A single power-law fitting is shown by the orange line, while the blue line is for a double power-law. In the latter case, the transitions are shown by the dashed vertical lines. As a comparison, the power-law with $\alpha = 1$ is shown by the dashed black line.

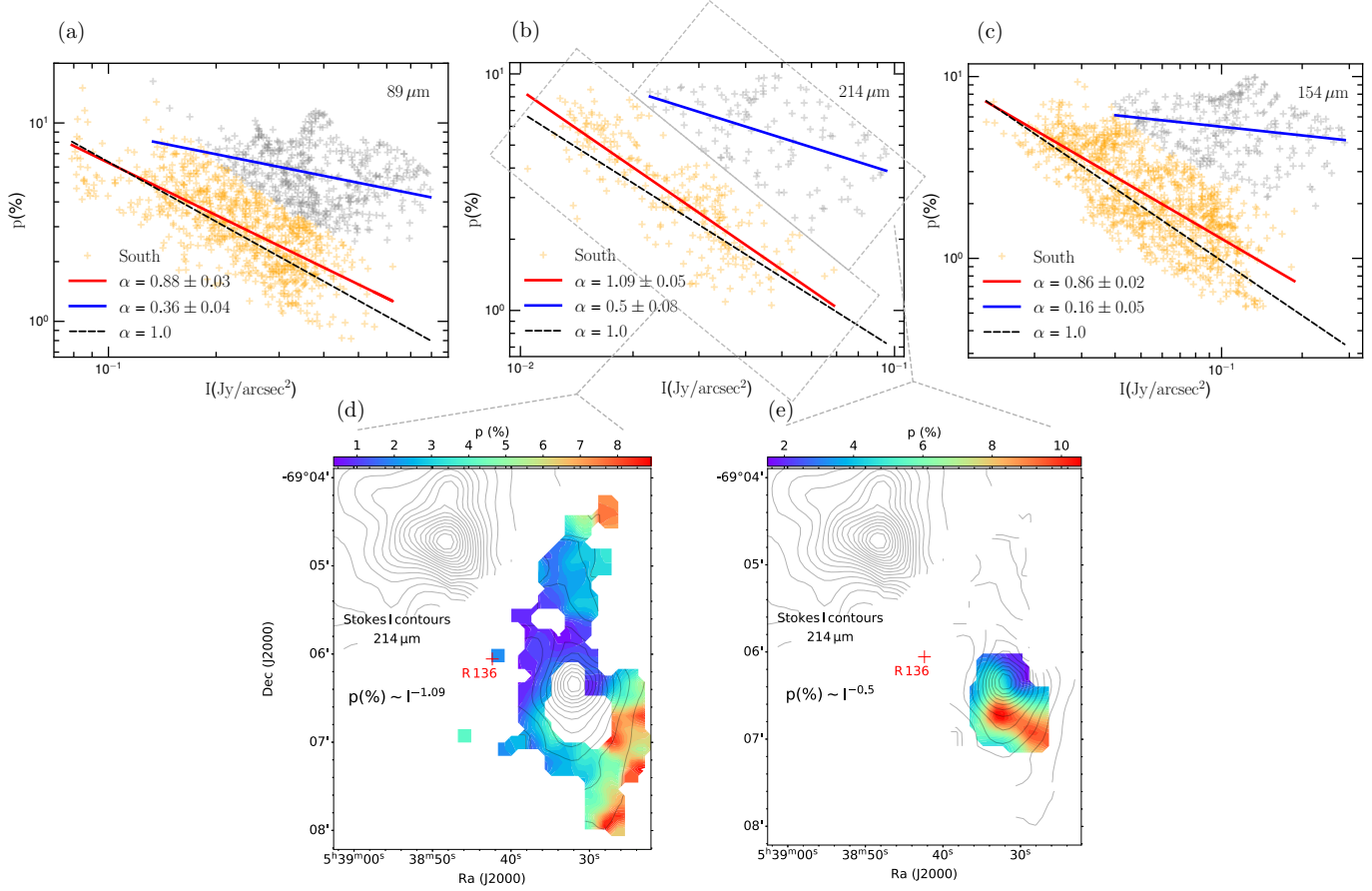


Figure 6. Similar to Figure 5 but for the South. The data points likely group separately, hence we classify them into two different clusters by using BAYESIANGAUSSIANMIXTURE library in python-package. These clusters are colored by the gray and orange points in panels (a,b,c), which are followed by the power-law fittings. The slope differs from one to another cluster, which indicates a distinguished grain alignment efficiency between the two regions. Panels(d,e) visualize the spatial distribution of these clusters. The slope is shallower at around the peaked intensity and gas column density, whereas the polarization decreases steeply to higher intensity.

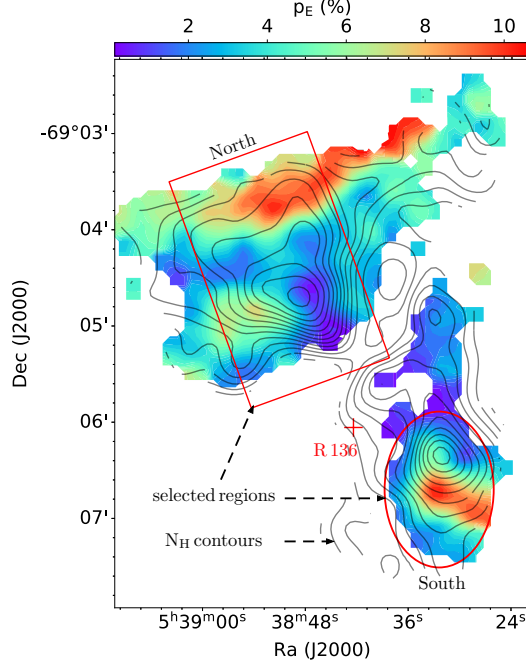


Figure 7. Sub-region selections. Background is the polarization degree at band E of the common space position which all SOFIA/HAWC+ detected data. The contours show the gas density map. The red rectangle (origin at $5^h38^m51.041^s - 69^{\circ}04'25.084''$, width= $17.12''$, height= $2.5'$) and ellipse (origin at $5^h38^m32.4^s - 69^{\circ}06'42''$, major axis = $6.05''$, minor axis = $0.81'$) show the selected regions, where we are interested in.

than that in the far-side region (lower and upper right corners; see color bars). The low polarization degree at higher radiation intensity is unexpected from the basic RAT alignment theory.

We note that the best-fits to the $p - I$ data only reflect the general trend and cannot describe accurately the underlying physics across the different regions. Indeed, as shown in Figure 5, there are many data points that appear to follow the steep slope of $\alpha = 1$ toward high intensity. This can also be seen from Figure 3c that the polarization degree is minimum around the central radiation source, while it becomes higher at the farthest side from this source where the dust temperature is relatively low (see Figure 3b,c,d). Therefore, in the next section, we will perform additional analysis of the polarization with the gas column density and dust temperature.

3.3. Polarization degree versus dust temperature and gas column density

For the optically thin case, the total dust emission intensity is $I_\nu \propto B(T_d)\tau_\nu \sim \kappa_\nu N_{\text{H}} B(T_d) \times R$ with R the dust-to-gas ratio and κ_ν the dust opacity, which is the product of the gas column density and dust temperature along the line of sight. Therefore, the $p - I$ relation reflects the overall effect of both the radiation field and the gas density on grain alignment, assuming a uniform average magnetic field. To disentangle the effect of the radiation field from the gas density, we analyze the variation of the polarization degree with the dust temperature and the gas column density. The first analysis directly reveals the grain alignment and disruption by RATs, while the second one reflects the effect of grain randomization induced by gas collisions.

To make comparison among 3 bands, we first smooth the maps of the dust temperature, gas column density, and SOFIA/HAWC+ bands C and D to the $18.7''$ FWHM, which is equivalent to the SOFIA/HAWC+ band E beam-size. Then, we selected the common space position where three SOFIA/HAWC+ bands all detect data. The final map is shown in Figure 7. From this final map, we analyze the correlations in two sub-regions: within a rectangle in the North, and within an ellipse in the South. These extraction areas cover the representative features of both the gas density and the dust temperature in 30 Dor, which are shown in Figure 7.

Figure 8 shows the two-dimensional histogram of the gas column density and the dust temperature relation for these two representative North (upper panel) and South (panel) regions. In the North, a PWLF fitting (Jekel & Venter 2019)

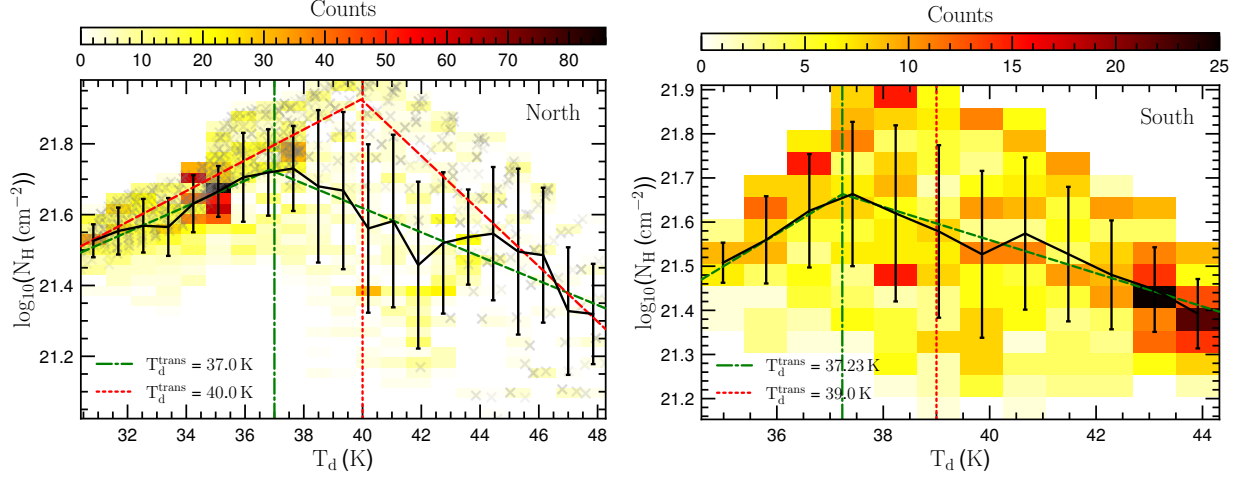


Figure 8. Relation of the gas column density and the dust temperature in the North region (upper panel) and in the South region (lower panel). They are positively correlated for $T_d < 37\text{ K}$, while they are negatively correlated for $T_d > 37\text{ K}$.

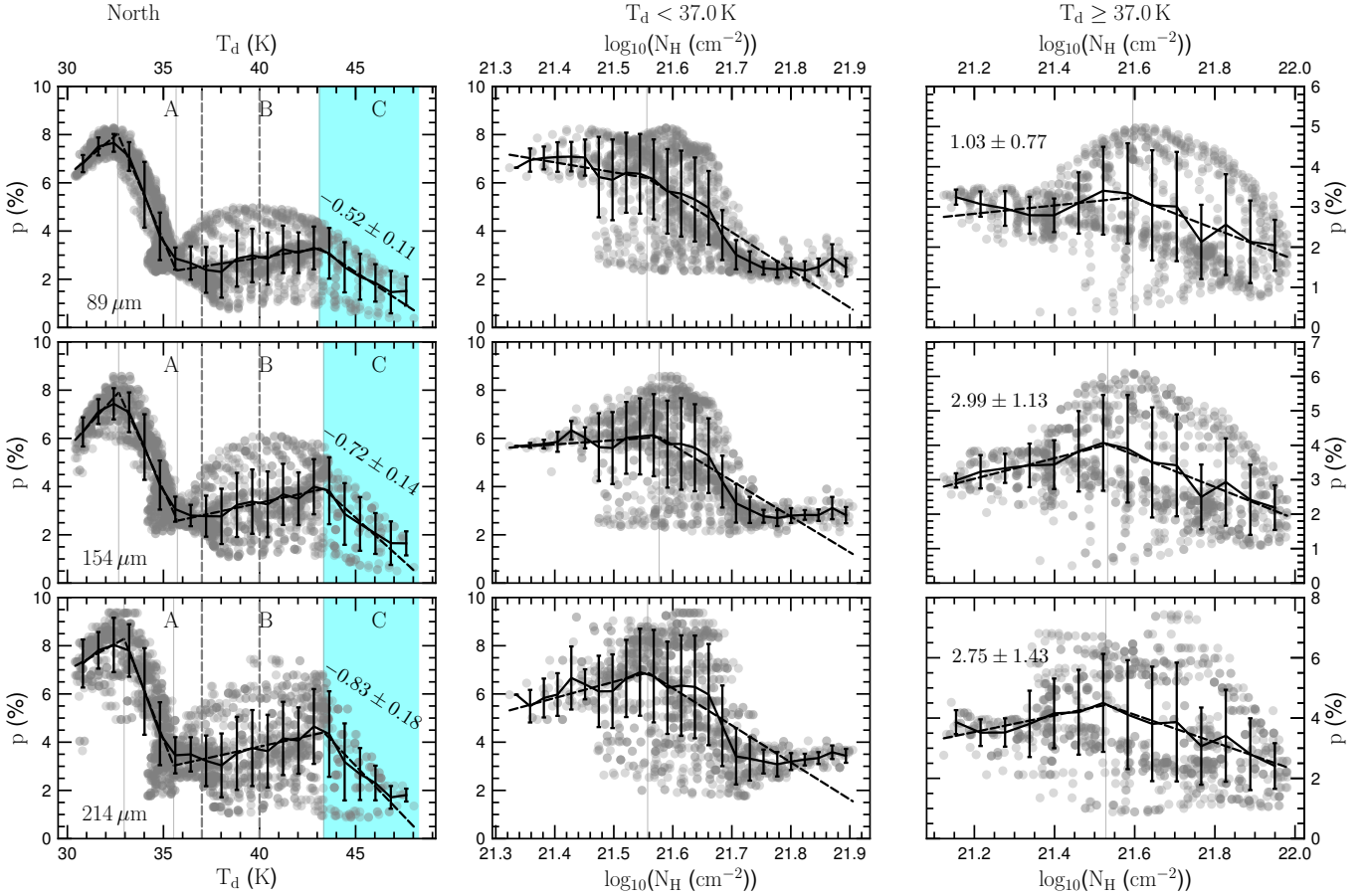


Figure 9. Left panel: correlation of the polarization degree to the dust temperature. Middle and right panels: correlation of the polarization to the gas column density within $T < 37\text{ K}$ and $T_d \geq 37\text{ K}$, respectively. Solid black line is the weighted-mean within $1 - \sigma$ uncertainty in each bin. Dashed black line is the piecewise line fitting. On the left column, the dashed vertical lines indicate the corresponding T_d^{trans} . The $p - T_d$ relation shows three features: p decreases (region A), slightly increases (region B), and decreases (region C) as T_d increases. The mean value of the slopes and their associated 95% level of confidences are given in region C.

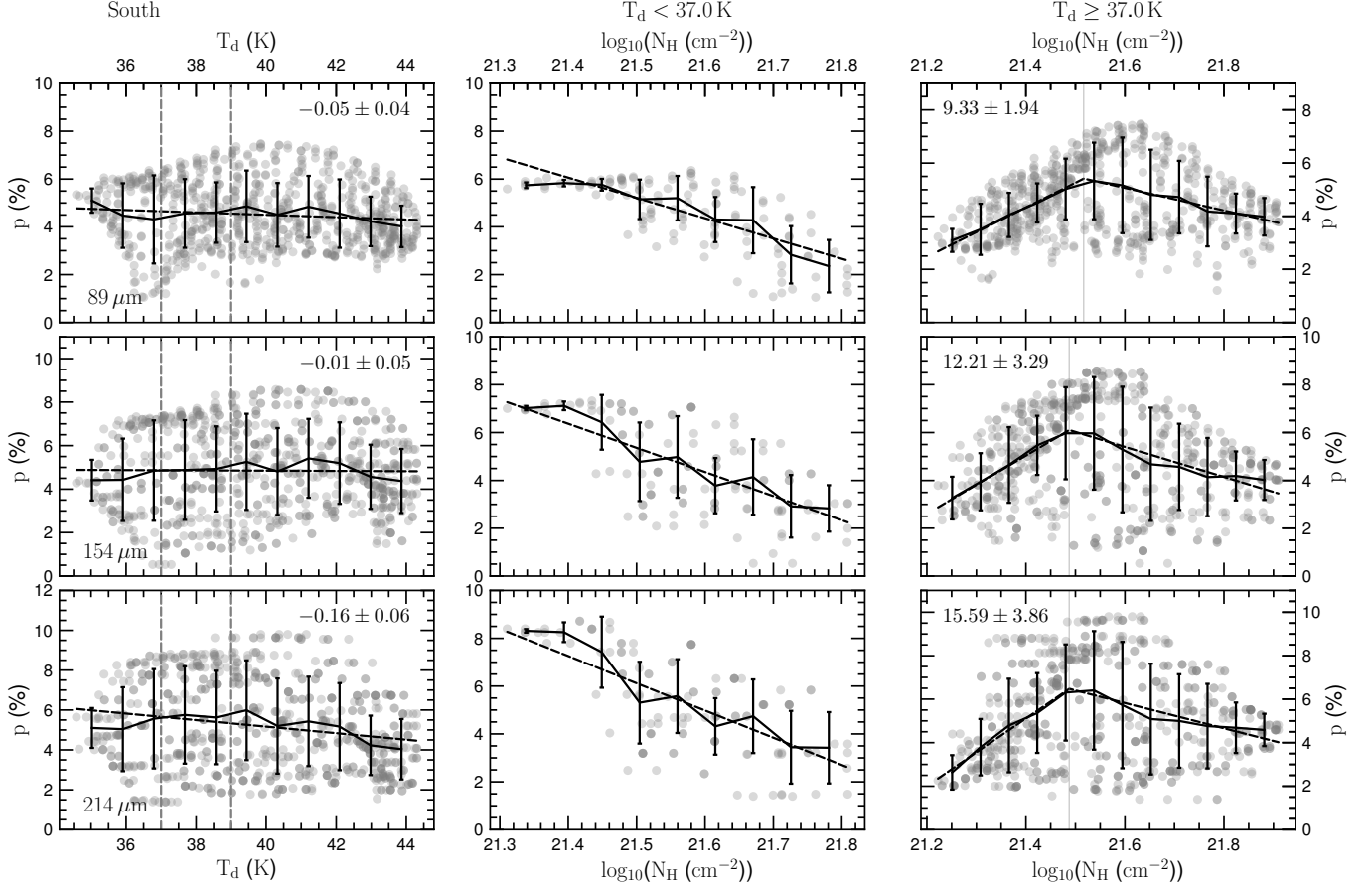


Figure 10. Similar to Figure 9 but for the South region. The polarization degree tends to decrease slowly with T_d (left panel). The polarization degree decreases with N_H for $T_d < 37\text{ K}$ (middle panel), but it increases and decreases with N_H for $T_d > 37\text{ K}$ (right panels).

to all data points shows the gas column density is positively proportional and then negatively proportional to the dust temperature, for which the dust is below and above $T_d^{\text{trans}} \simeq 37\text{ K}$. However, since the error bar is significantly large, we fit an upper envelope of the distribution and obtain a slightly higher value of $T_d^{\text{trans}} \simeq 40\text{ K}$. In the South, the transition temperature occurs around $37 - 39\text{ K}$. However, the plot is much more scattered than in the North.

In Figure 9, we show the relations of the polarization degree in 3 bands to the dust temperature (left panels from top to bottom). The black line shows the weighted mean fit (filled dots), and the black dashed line shows the piecewise line fit to the data. The separation owing to the $T_d - N_H$ is shown by two vertical dashed lines. The corresponding relations to the gas column density are shown in the middle and right panels, respectively. Notably, we only show the separation for $T_d^{\text{trans}} \simeq 37\text{ K}$ here because the behavior is the same for any values in between 37 K and 40 K .

For $T_d \leq 37\text{ K} - 40\text{ K}$, in which the dust temperature and the gas column density both increase toward the R 136, the polarization degree rapidly increases, then decreases and finally gets nearly plateau with increasing dust temperature (region A in left panels). Meanwhile, the polarization degree tends to decrease up to $N_H \sim 10^{21.7}\text{ cm}^{-2}$ and gets plateau with increasing the gas column density (middle panels).

For $T_d > 37\text{ K} - 40\text{ K}$, in which the dust temperature and the gas column density are anti-correlated toward the R 136, the polarization degree first increases slightly and then decreases with increasing both the dust temperature (region B and C in left panels) and the gas column density (right panels). Furthermore, the declining slope of $p - T_d$ is steeper for the longer wavelength, i.e., the mean slope of -0.52 at $89\text{ }\mu\text{m}$, -0.72 at $154\text{ }\mu\text{m}$ and -0.83 at $214\text{ }\mu\text{m}$.

Similarly, Figure 10 shows the correlations of the polarization degree to the dust temperature and the gas column density in the South region. Although these plots are scattered, one can see a weak correlation between the polarization degree with the dust temperature. The relation to the gas column density is also separated for the different range of dust temperature according to Figure 8. The relation to the gas column density looks somehow similar to the middle

and right panels of Figure 9. For $T_d < 37 - 39$ K (middle panel), the polarization degree shows a monotonic decrease with increasing the column density. However, for $T_d \geq 37 - 39$ K (right panel), the polarization degree first increases and then decreases with increasing the column density, as seen in the North region.

In summary, the $p - T_d$ and $p - N_H$ relations are not monotonic as in $p - I$. The most interesting feature is the anti-correlation of p vs. T_d and the correlation of p with N_H , which cannot be explained by the basic RAT alignment theory alone.

4. DISCUSSION

In this section, we will discuss the implications of the observed $p - I$, $p - T_d$, and $p - N_H$ relations for the leading theory of grain alignment and disruption based on RATs.

4.1. On the $p - I$ relation and grain alignment

The variation of the polarization degree of thermal dust emission with the total emission intensity (I) is a popular analysis of polarimetric data, which provides information on grain alignment and magnetic fields. Numerous studies show that the polarization decreases with I as $p \propto I^{-\alpha}$ with the slope $\alpha \simeq 0 - 1$. If grain alignment and the magnetic field are uniform throughout the cloud, one expects $\alpha = 0$. If grain alignment only occurs in the outer layer and becomes completely lost in the inner region, one expects $\alpha = 1$ (Whittet et al. 2008). The latter slope is previously reported in the case of starless cores (see e.g., Crutcher et al. 2004; Alves et al. 2014; Jones et al. 2015). Theoretically, for uniform grain alignment in the cloud, the stochastic magnetic field is found to induce a slope of $\alpha = 0.5$ (see Jones et al. 1992, 2015).

In Section 3.2, we showed the $p - I$ diagrams in all 3 bands in both North and South regions. In the North, a single power-law fitting shows that the diagram at $89 \mu\text{m}$ has a steep slope of $\alpha > 0.5$, while the ones at longer wavelengths show a shallower slope of $\alpha < 0.5$. The slope of $p - I$ relations seem rather low compared to other regions, e.g., Auriga-California cloud ($\alpha \simeq 0.82$, Ngoc et al. 2021), Perseus B1 ($\alpha \simeq 0.8$, Coudé et al. 2019), Ophiuchus B, C ($\alpha \simeq 0.6 - 0.7$, Pattle et al. 2019), Serpens South ($\alpha \simeq 0.55$, Pillai et al. 2020). A double power-law fitting indicates the diagrams change from the first, steep slope of $\alpha > 0.5$ to the second, shallower slope of $\alpha < 0.5$ toward the peak dust emission intensity. This transition feature seems similar to the case of NGC 6334 (Arzoumanian et al. 2020). In both cases, the shallow slope of the $p - I$ diagram is shown, which can be explained by the high grain alignment efficiency by RATs owing to the intense radiation flux from the luminous source R 136.

Indeed, according to the RAT alignment theory, the degree of dust polarization is determined by the minimum size of aligned grains (a_{align}). A smaller value of a_{align} results in a higher p because the size distribution of aligned grains (i.e., from a_{align} to the maximum grain size (a_{max}))) is broader. Similarly, a larger value of a_{align} causes the lower polarization due to a narrower size distribution of aligned grains, assuming that a_{max} is fixed (without RATD). The alignment size depends on the local physical conditions as $a_{\text{align}} \sim n_H^{2/7} T_d^{-12/7}$ (see Equation A1).

Since 30 Dor is a complex region, it is very difficult to accurately constrain the local physical properties such as n_H and T_d (see Okada et al. 2019). Therefore, in Figure 11, we show the map of a_{align} with respect to T_d and n_H . The values of n_H span broadly from 10^3 to 10^6 cm^{-3} (see Chevance et al. 2016 and Lee et al. 2019), while that of T_d is adopted from observations (Figure 3d). The alignment size increases with increasing gas density and decreasing dust temperature (from upper left corner to lower right corner). For a given dust temperature, a_{align} becomes larger for higher gas density (from left panel to right panel), which arises from the increase of the collisional disalignment rate with the gas density.

In the case of two slopes, when approaching the luminous source of R 136, the local dust temperature (i.e., radiation strength) increases, which significantly decreases a_{align} (see Figure 11). As a result the polarization degree of thermal dust emission increases (Hoang et al. 2021). This can reproduce the shallow slope of $\alpha \sim 0.3 - 0.4$ observed toward the peak intensity. For the first steep slope of $\alpha > 0.5$, the alignment size increases due to the decrease of the interstellar radiation field as well as (the collisional damping becomes more significant), and one expects the slope of $\alpha = 1$ when grain alignment is completely lost. However, if grain growth occurs, the size distribution of aligned grains ($a \sim a_{\text{align}} - a_{\text{max}}$) is still finite, which can produce the slope shallower than $\alpha \sim 1$ (see Hoang et al. 2021). Incidentally, the optical to near-infrared observations of 30 Dor by *Hubble Space Telescope* (De Marchi & Panagia 2014) reported a high value of the ratio of the total and selective extinction R_V as 4.4, which implies the grain growth in 30 Dor. Other effects, including the tangling of the magnetic fields, can also reproduce the first slope.

In the South, the $p - I$ diagrams illustrate two clusters with different properties. The first group shows a quite shallow slope with $\alpha \simeq 0.2 - 0.5$ at around the peak of the intensity and gas column density, which is opposite to the

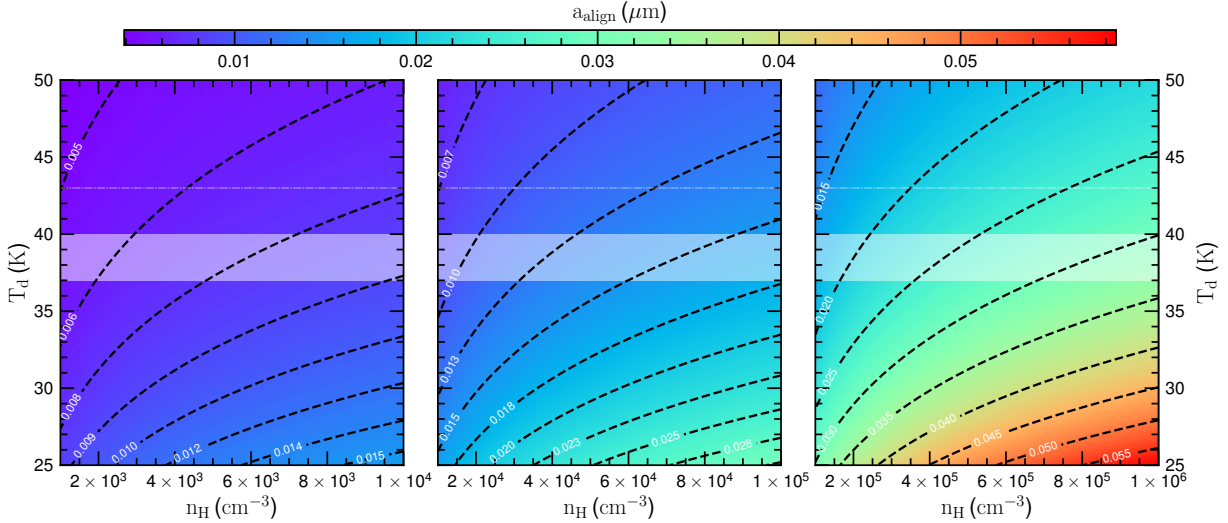


Figure 11. The alignment size (minimum size of aligned grains by RATs, a_{align}) as functions of the dust temperature (T_{d}) and the gas volume density (n_{H}) computed with $\bar{\lambda} = 0.3$, $\gamma = 1$, and $T_{\text{gas}} = T_{\text{d}}$. The alignment size is larger (smaller) for higher (lower) gas density and lower (higher) dust temperature. The white region shows the range of the transition temperature ($T_{\text{d}}^{\text{trans}}$).

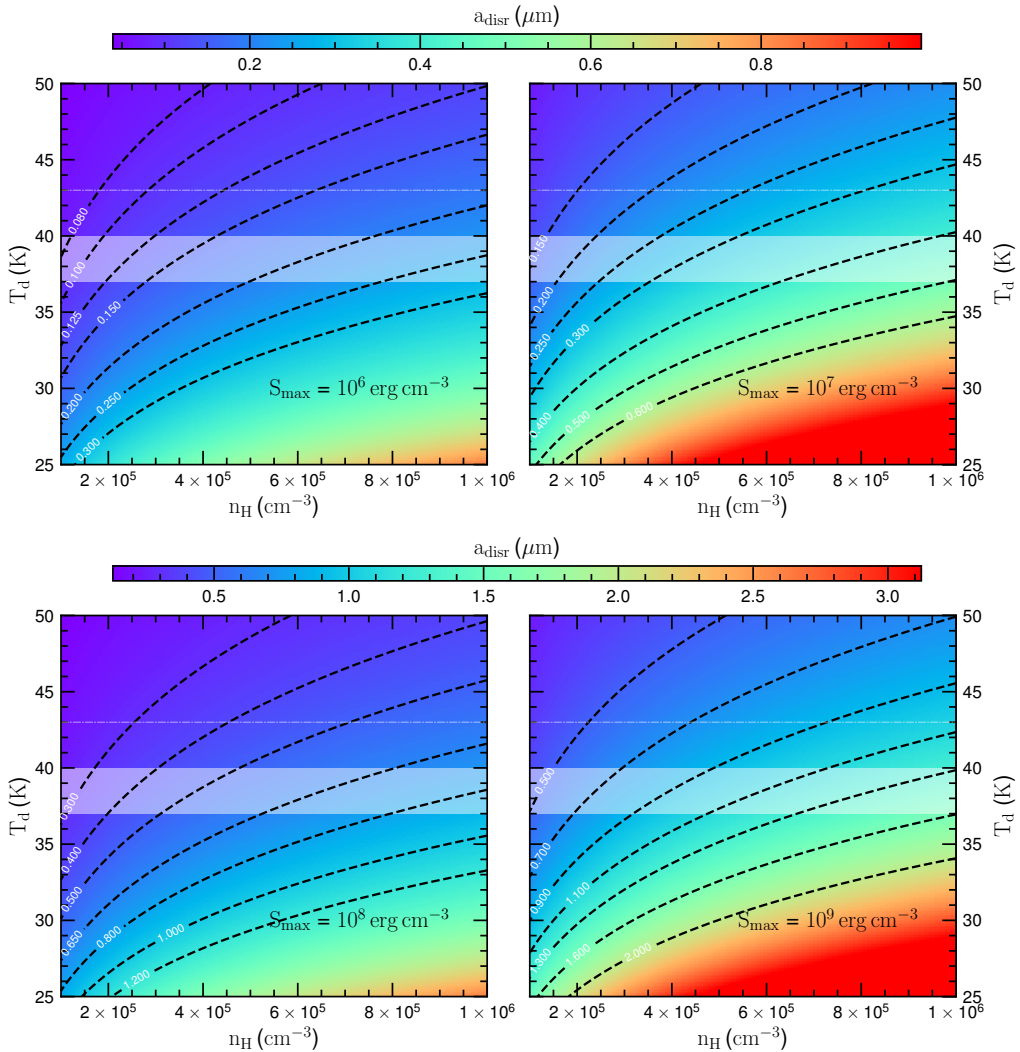


Figure 12. Similar to Figure 11 but for the grain disruption size (a_{align}) for different values of the tensile strength (S_{max}). a_{disr} is smaller (larger) for higher (lower) T_{d} and lower (higher) n_{H} . For the same physical condition, a_{disr} is larger for higher S_{max} . In each panel, the white dashed horizontal line represents $T_{\text{d}} = 43$ K.

North. The second group otherwise shows a very deep slope as $\alpha \simeq 1$. Naturally, the contradiction of the polarization degree reflects a difference in the radiation flux and the grain size distribution. However, the dust temperature is not the highest at the dense gas (Figure 3d). Thus, it is likely that grains are larger in the dense region and responsible for a shallow slope of the $p - I$ diagram.

The North and South regions share a common feature that the polarization degree seems to be larger at greater distances from the central source with a low gas density and low dust temperature. An interesting feature is that the polarization degree appears to be low in the vicinity of R136, in which the radiation is strong and the gas density is not the densest (Figure 3c). This is evidence in support of the RATD mechanism, which will be discussed in detail in the next section.

4.2. On the $p - T_d$ and $p - N_H$ relations and grain alignment

As shown in Figure 9, the variation of p with T_d and N_H in the North region is more complex than the $p - I$ relation. For $T_d \leq 37\text{ K}$, p decreases with increasing T_d (left panels) and N_H (middle panels). For $T_d > 37\text{ K}$, p first increases with increasing T_d and N_H , then decreases when T_d becomes sufficiently large (see B and C regions in the left panels). The increase of p with T_d and the decrease of p with N_H are expected from the RAT alignment theory as the alignment size decreases with increasing U and decreasing n_H (see Figure 11, also Equation A1). However, the decrease of p with T_d is unexpected from the basic RAT alignment theory because the alignment size a_{align} is smaller for larger T_d (U). Similarly, the increase of p with N_H is unexpected because a_{align} increases with the gas density.

In the South, the relations of p to T_d and N_H are more scattered and not very obvious as shown in Figure 10. However, the South is likely closer to R136 than the North, and the selected area covers mostly the region where the grain alignment efficiency is high. However, the polarization degree seems to not vary with T_d and decreases with decreasing the gas column density for $T_d > T_d^{\text{trans}}$. Same as in the North, the latter trend is opposite to the expectation by the basic RAT alignment theory.

4.3. A new evidence of the RATD mechanism

In Figure 9 and 10, we found that the polarization degree first increases and then decreases as the dust temperature increases and the gas column density decreases (region C in Figure 9) for $T_d > 43\text{ K}$. The decrease of p with T_d (higher radiation flux, closer R136) and the increase of p with decreasing N_H cannot be explained by the basic RAT alignment theory, as discussed in the previous subsection, unless the increasing dust heating is associated with the increase in the tangling of the magnetic field. Below, we suggest that the combination of the RAT alignment with the RATD mechanism (Hoang et al. 2019) can reproduce this feature.

According to the RATD mechanism, dust grains subject to a strong radiation field (i.e., close the source R136) can be spun-up to extremely fast rotation. The induced centrifugal stress due to grain suprathermal rotation can exceed the tensile strength of the grain material, resulting in the spontaneous fragmentation of large grains into smaller ones. The depletion of large grains causes the decrease of the thermal dust polarization degree at long wavelengths (see Lee et al. 2020; Tram et al. 2021a).

To study if RATD can reproduce the observed anti-correlation of $p - T_d$, let us estimate the critical size above which dust grains are disrupted, a_{disr} . The disruption size depends on the local conditions and the grain structure as $a_{\text{disr}} \sim n_H^{1/2} T_d^{-3} S_{\text{max}}^{1/4}$ (see Section B). As shown in Tram et al. (2021a,b), the disruption occurs at the critical disruption temperature of $T_d^{\text{disr}} \simeq 32\text{ K}$ for $n_H \simeq 10^5 \text{ cm}^{-3}$, and $T_d^{\text{disr}} \simeq 71\text{ K}$ for $n_H \sim 10^6 \text{ cm}^{-3}$. Thus, the gas volume density in the region within $43 \leq T_d < 50\text{ K}$ could be in $(10^5 - 10^6 \text{ cm}^{-3})$ interval. Figure 12 shows the map of the grain disruption size as a function of T_d and n_H for different value of S_{max} . Grains within composite structure ($S_{\text{max}} \sim 10^5 - 10^7 \text{ erg cm}^{-3}$) are being disrupted at smaller size than the more compact grains (higher value of S_{max}). For instance, for $n_H = 6 \times 10^5 \text{ cm}^{-3}$ and $T_d = 43\text{ K}$, $a_{\text{disr}} = 0.15, 0.26, 0.46, 0.82 \mu\text{m}$ for $S_{\text{max}} = 10^6, 10^7, 10^8, 10^9 \text{ erg cm}^{-3}$, respectively. Thus, the RATD mechanism can reasonably disrupt the composite grains for $T_d \geq 43\text{ K}$. The disruption size gets smaller for higher T_d .

Figure 13 sketches our understanding on the main feature of dust polarization in 30 Dor expected from theoretical modeling of dust polarization based on grain alignment and disruption by RATs (Lee et al. 2020). For an illustration, a color map of a_{align} (in arbitrary units) is shown as functions of T_d and n_H . The feature of p fundamentally depends on the $T_d - n_H$ relation. If we assume $n_H \sim N_H$ maps (e.g., the local variation of the depth of cloud is significantly small or negligible), the observed polarization degree (p) profile could be explained in three ranges of T_d .

For $T_d < T_d^{\text{trans}}$ (at which the $T_d - n_H$ relation changes the sign from positive to negative, see Figure 8), T_d positively correlates to n_H . If the gas density increases faster than the radiation strength ($U \propto T_d^6$), such that the rotational

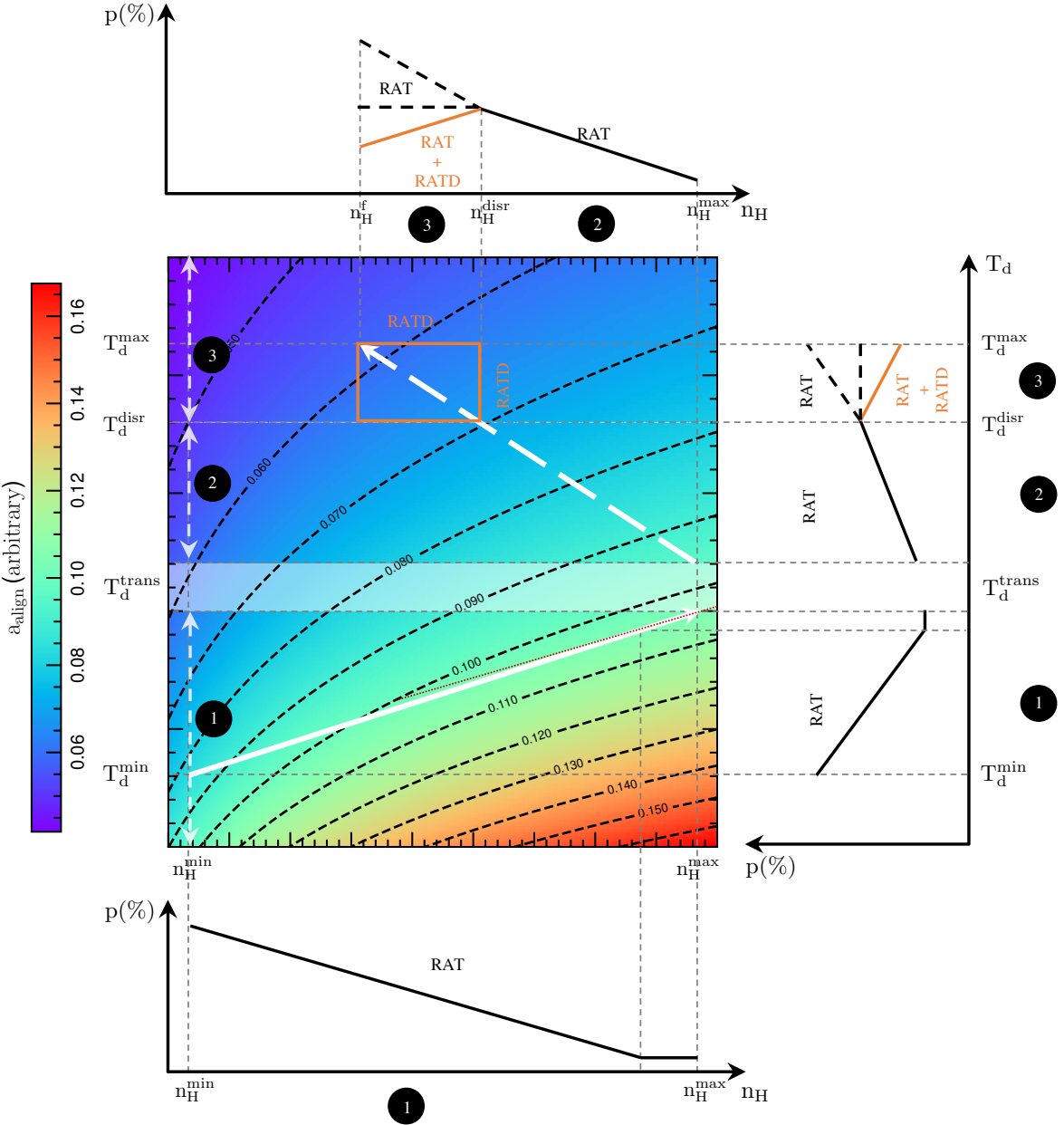


Figure 13. Understanding the thermal dust polarization in 30 Dor in the light of RAT alignment and RATD. According to the RAT alignment theory, the polarization degree is determined by the grain alignment size (a_{align}), which depends on the dust temperature (T_d) and the gas volume density (n_H). Therefore, the observed $p - T_d$ and $p - n_H$ trends could be explained by three distinct stages denoted by ①, ②, and ③. For ① with $T_d < T_d^{\text{trans}}$, T_d is positively proportional to n_H (solid white arrow), the grain alignment size increases along this direction only if n_H increases faster than the radiation strength $U \propto T_d^6$, which results in the decrease of the polarization degree (p) with both T_d and n_H . If T_d increases such that U increases faster than n_H , one expects p to go up. For ② with $T_d > T_d^{\text{trans}}$, T_d is negatively proportional to n_H (dashed white arrow), p increases with increasing T_d and decreasing n_H as a_{align} becomes smaller along this direction. Finally, for ③ with $T_d > T_d^{\text{disr}}$, the RATD effect becomes active, resulting in the drop of p toward higher T_d and lower n_H (orange lines), which explains the observed trend. Without RATD, p is expected to continue increasing or be constant. Therefore, the joint effect of grain alignment and disruption by RATs can successfully explain the observed polarized thermal dust emission of 30 Dor.

damping by gas collisions is sufficiently strong to prevent the grains from being spun-up to the disruption limit by RATs, a_{align} is larger with increasing T_d and n_H (solid white arrow). This increment of a_{align} consequently causes the polarization degree to decrease to both the dust temperature and gas density as expected from the RAT alignment theory. In this case, a_{align} might also become constant with a specific range of T_d and n_H because of their opposite effect. These features explain the observed region A of $p - T_d$ in Figure 9 and $p - N_H$ in the middle panel of Figures 9, 10. In the case if the dust temperature increases such that U increases faster than the gas density, the rotational damping by gas collisions is insufficiently strong to prevent the grains from being spun-up by RATs, a_{align} is getting smaller as T_d and n_H increase. Thus, the polarization degree is increasing instead of decreasing, which contradicts to the observed trend of 30 Dor.

For $T_d > T_d^{\text{trans}}$, T_d and n_H are anti-correlated (see Figure 8). The gas collision damping is further weak, the grain alignment size gets smaller as T_d increases (dashed white arrow). Thus, the polarization degree gets increased toward higher T_d and lower n_H . This feature could explain the region B of the observed $p - T_d$ in Figure 9.

For $T_d > T_d^{\text{disr}}$, the depletion of large grains due to the RATD mechanism results in the decrease of the polarization degree toward higher T_d and lower n_H . This feature successfully reproduces the observed $p - T_d$ in region C of Figure 9 and $p - N_H$ in the right panels of Figures 9, 10. Otherwise, the polarization degree is expected to continuously increase or at least flat accordingly to the RAT alignment theory (see Lee et al. 2020).

However, there is a question remaining why the relation of p to T_d is weak in the South. This slow variation may be due to the saturation of RATD, which occurs when $T_d \gg T_{\text{disr}}$ (see Figure 14 in Lee et al. 2020). Induced small grains likely have compact structures and RATD ceases to act at some high T_d . Furthermore, when T_d is large, IR damping is so strong that a_{disr} becomes to slowly change with T_d . Both effects induce the slow variation of p with T_d .

Previous studies have reported the anti-correlation of the dust polarization with grain temperature for several molecular clouds (Planck Collaboration et al. 2020), the ρ Ophiuchus A which is irradiated by a nearby B-association star (Santos et al. 2019; Tram et al. 2021a)³, and at 89, 154, 214, and 850 μm of a cloud surrounding the massive star BN/KL (Tram et al. 2021b). Numerical modeling studies (Lee et al. 2020) show that the RATD mechanism (Hoang 2020) could successfully reproduce the observed anti-correlation of the polarization with grain temperature at the same FIR and submm wavelength ranges. The observed anti-correlation of $p - T_d$ in 30 Dor is a new evidence for the RATD mechanism.

4.4. Dust polarization mechanisms

Our analysis so far is focused on the polarization degree with the assumption that far-IR dust polarization is induced by dust grains aligned with a preferred direction. Modern theory of RAT alignment theory implies that such a preferred axis could be the magnetic field (B-RAT) or the radiation direction (k-RAT) (Lazarian & Hoang 2007). As a result, the polarization vectors of polarized thermal emission are perpendicular to the magnetic field (radiation direction). The B-RAT alignment is most likely in the diffuse ISM and molecular clouds, whereas the k-RAT can occur near a strong radiation source where the rate of grain precession around the radiation direction is larger than the Larmor precession around the magnetic field (Hoang & Lazarian 2016; Lazarian & Hoang 2019). In this case, the polarization vectors of thermal dust emission are perpendicular to the radiation direction. Therefore, the polarization vectors provide valuable constraints on dust magnetic properties and alignment mechanisms (Chuss et al. 2019; Lazarian & Hoang 2019; Pattle et al. 2021).

In the South region of Figure 2, the polarization vectors (the E-vectors) appear to be concentric with respect to the intense source R136. Such a polarization pattern is different from the one in the North region which is far from the source R136 where grains are most likely aligned via B-RAT. This indicates that the alignment mechanisms in the South may be due to the alignment with the radiation direction. Evidence for k-RAT is previously reported for some star-forming regions (Chuss et al. 2019; Pattle et al. 2021) and protoplanetary disks (Kataoka et al. 2017; Stephens et al. 2017). We will study in detail this issue in a follow up paper on 30 Dor.

5. SUMMARY

In this paper, we report our results analyzing the far-IR polarimetric observations of 30 Doradus by SOFIA/HAWC+. 30 Dor cloud is located in the Large Magellanic Cloud and mainly irradiated by an intense radiation source from the massive R136 cluster. Thus, this region is an ideal target to study the physics of grain alignment and disruption driven

³ In the case of ρ Ophiuchus A, the observed trend of $p - T_d$ is explained by the processes ② and ③ in Figure 13.

by RATs. To infer the alignment and disruption properties of dust grains, we have performed three different analyses based on the polarization degree, including $p - I$, $p - N_{\text{H}}$, and $p - T_{\text{d}}$. Our main findings are summarized as bellows

- 1 The thermal dust polarization varies across the 30 Dor cloud, in which there are two main regions, namely North and South in relative to the massive star cluster R136. In the North region, the polarization patterns are likely radial from R136 within the polarization angle peaked at $\simeq 20^\circ$, while they are concentric around R136 within the peaked polarization angle of $\simeq -60^\circ$ in the South region.
- 2 For the North region, a single power-law fitting show a shallow slope of the $p - I$ diagrams, which could be explained by an intense radiation field. A double power-law fitting shows a change from a steeper slope of $\alpha > 0.5$ to a shallower slope as $\simeq I^{-0.4} - I^{-0.3}$ toward higher intensity. The latter shallow slope most likely arises from the enhanced alignment of grains by RATs when approaching the source R136.
- 3 The variations of the polarization degree with the dust temperature and gas column density in the North are complex. The polarization degree decreases with increasing the dust temperature and the gas column density for $T_{\text{d}} < 37 \text{ K}$, which might result from the loss of grain alignment due to strong collisional damping by denser gas. For $T_{\text{d}} > 37 \text{ K}$, the polarization degree increases as the dust temperature increases and the gas column density decreases. However, the polarization degree decreases as the dust temperature increases beyond $\sim 43 \text{ K}$ and the gas column density further decreases. Such an anti-correlation of $p - T_{\text{d}}$ is consistent with the prediction of the RATD theory that the dust polarization decreases due to disruption of large grains toward the intense radiation source R136.
- 4 In the South region, the polarization degree is higher, and the $p - I$ slope is shallower at the peak of the intensity and gas column density. Whereas, the polarization degree is the highest at further away (low intensity and less dense gas) and decreases steeply as $p \propto I^{-1}$ backward to R136 (higher intensity and denser gas). The first feature is likely caused by enhancement of grain alignment by RATs due to the radiation from the source R136. The second feature is unexpected from the basic RAT alignment theory, but is consistent with the prediction by the RATD effect, as in the North.
- 5 In the South, the stronger grain randomization by gas collisions in the densest part results in a weak correlation of the polarization degree to the dust temperature. Whereas, the polarization degree likely decreases toward low and high gas column density. However, the relations are quite scattered and show a large error bar.

The values of the dust temperature and gas column density using in this work are derived from the modified black-body fitting to the *Herschel* data, and they thus encompass the projection effect. Our conclusions are given without taking the B-field tangling into account. The variation of the magnetic field could result in the modification of the grain alignment and then the polarization degree. Despite these aspects, our SOFIA/HAWC+ data show that the grain alignment is complicate and significantly varied across the 30 Dor cloud, and evidence a strong impact of the intense radiation field of a massive star cluster R136. The drop of the polarization degree as close to the central source, in which the gas column density is not peaked, is contrary to the RAT alignment theory. The lower abundance of large grains via the disruption mechanism by radiative torque could be responsible for this declination.

Acknowledgments: We thank the anonymous referee for a helpful report. This research is based on observations made with the NASA/DLR Stratospheric Observatory for Infrared Astronomy (SOFIA). SOFIA is jointly operated by the Universities Space Research Association, Inc. (USRA), under NASA contract NNA17BF53C, and the Deutsches SOFIA Institut (DSI) under DLR contract 50 OK 0901 to the University of Stuttgart. Financial support for this work was provided by NASA through award 4-0152 issued by USRA. T.H is funded by the National Research Foundation of Korea (NRF) grant funded by the Korea government (MSIT) through the Mid-career Research Program (2019R1A2C1087045).

Facility: SOFIA

APPENDIX

A. GRAIN ALIGNMENT SIZE

Grains are effectively aligned only when they can rotate suprathermally, i.e., the grain angular velocity (ω) is greater than the thermal velocity (ω_T) (Hoang & Lazarian 2008; Hoang & Lazarian 2016). The minimum alignment size (a_{align}) above which grains are aligned can be computed as $\omega(a_{\text{align}}) \equiv 3 \times \omega_T$. As exposed to a radiation source, the minimum a_{align} is determined analytically as (see Equation 26 in Hoang et al. 2021)

$$a_{\text{align}} \simeq 0.055 \hat{\rho}^{-1/7} \left(\frac{\gamma}{0.1} \right)^{-2/7} \left(\frac{n_H}{10^3 \text{ cm}^{-3}} \right)^{2/7} U^{-2/7} \quad (\text{A1})$$

$$\left(\frac{T_{\text{gas}}}{10 \text{ K}} \right)^{2/7} \left(\frac{\bar{\lambda}}{1.2 \mu\text{m}} \right)^{4/7} (1 + F_{\text{IR}})^{2/7} \quad \mu\text{m},$$

where γ is the anisotropy degree, $\bar{\lambda}$ is the mean wavelength, and U^4 is the strength of the radiation field, respectively. n_H and T_{gas} are the number density and temperature of the gas. F_{IR} is the ratio of the IR damping to the collisional damping rate. If we use $U \simeq (T_d/16.4 \text{ K})^6$ (Draine 2011), one can see that the alignment size depends on the local properties as $a_{\text{align}} \sim n_H^{2/7} T_d^{-12/7}$. The alignment size decreases (increases) with decreasing (increasing) gas density and increasing (decreasing) dust temperature as shown in Figure 11.

B. GRAIN DISRUPTION SIZE

Large grains exposed to an intense radiation field can be spun-up to extremely fast due to RATs. The fast rotation induces a strong centrifugal stress which opposes the binding energy that holds up the grain structure (i.e., tensile strength). Once the centrifugal stress exceeds the tensile strength, the grain is spontaneously fragmented. This fragmentation is called Radiative torque disruption (RATD). The critical grain size above which grains will be disrupted by the RATD mechanism is

$$a_{\text{disr}} \simeq 0.22 \hat{\rho}^{-1/4} \gamma^{-1/2} \left(\frac{n_H}{10^3 \text{ cm}^{-3}} \right)^{1/2} U^{-1/2} \left(\frac{T_{\text{gas}}}{10 \text{ K}} \right)^{1/4} \quad (\text{B2})$$

$$\times \left(\frac{\bar{\lambda}}{0.5 \mu\text{m}} \right) \left(\frac{S_{\text{max}}}{10^7 \text{ erg cm}^{-3}} \right)^{1/4} (1 + F_{\text{IR}})^{1/2} \quad \mu\text{m},$$

where S_{max} is the tensile strength which is determined by the internal structure of dust grains (see Equation 30 in Hoang et al. 2021). The compact grains have a higher tensile strength and are stronger than the composite ones (see Hoang 2019). One can see that $a_{\text{disr}} \sim n_H^{1/2} T_d^{-3} S_{\text{max}}^{1/4}$, which illustrates that the disruption size also decreases (increases) with decreasing (increasing) gas density and increasing (decreasing) dust temperature. Moreover, at the same local condition, grains within a weaker structure are easier to be disrupted than the stronger one as shown in Figure 12.

REFERENCES

- Alves, F. O., Frau, P., Girart, J. M., et al. 2014, A&A, 569, L1
- Andersson, B. G., Lazarian, A., & Vaillancourt, J. E. 2015, ARA&A, 53, 501
- Arzoumanian, D., Furuya, R., Hasegawa, T., et al. 2020, arXiv e-prints, arXiv:2012.13060
- Bernard, J.-P., Reach, W. T., Paradis, D., et al. 2008, AJ, 136, 919
- Chevance, M., Madden, S. C., Lebouteiller, V., et al. 2016, A&A, 590, A36
- Chuss, D. T., Andersson, B.-G., Bally, J., et al. 2019, ApJ, 872, 187. doi:10.3847/1538-4357/aaf37
- Coudé, S., Bastien, P., Houde, M., et al. 2019, ApJ, 877, 88
- Crutcher, R. M., Nutter, D. J., Ward-Thompson, D., & Kirk, J. M. 2004, ApJ, 600, 279
- De Marchi, G., & Panagia, N. 2014, MNRAS, 445, 93
- De Marchi, G., Paresce, F., Panagia, N., et al. 2011, ApJ, 739, 27
- Dolginov, A. Z., & Mytrophanov, I. G. 1976, Ap&SS, 43, 257
- ⁴ $U = u_{\text{rad}}/u_{\text{ISRF}}$, with $u_{\text{rad}} = \int u_\lambda d\lambda$ the radiation energy density of the local radiation field and $u_{\text{ISRF}} \approx 8.64 \times 10^{-13} \text{ erg cm}^{-3}$ the radiation energy density of the local interstellar radiation field (Mathis et al. 1984)
- Draine, B. T. 1980, ApJ, 241, 1021

- Draine, B. T. & Weingartner, J. C. 1996, ApJ, 470, 551.
doi:10.1086/177887
- . 2011, Physics of the Interstellar and Intergalactic Medium
- Dufour, R. J., Shields, G. A., & Talbot, R. J., J. 1982, ApJ, 252, 461
- Fissel, L. M., Ade, P. A. R., Angilè, F. E., et al. 2016, ApJ, 824, 134
- Galliano, F., Madden, S. C., Tielens, A. G. G. M., Peeters, E., & Jones, A. P. 2008b, ApJ, 679, 310
- Gordon, K. D., Roman-Duval, J., Bot, C., et al. 2014, ApJ, 797, 85
- Gordon, M. S., Lopez-Rodriguez, E., Andersson, B. G., et al. 2018, arXiv e-prints, arXiv:1811.03100
- Harper, D. A., Runyan, M. C., Dowell, C. D., et al. 2018, Journal of Astronomical Instrumentation, 7, 1840008
- Hoang, T. 2019, ApJ, 876, 13
- Hoang, T. 2020, Galaxies, 8, 52
- Hoang, T., & Lazarian, A. 2008, MNRAS, 388, 117
- Hoang, T. & Lazarian, A. 2016, ApJ, 831, 159.
doi:10.3847/0004-637X/831/2/159
- Hoang, T., & Tram, L. N. 2019, ApJ, 877, 36
- Hoang, T., Tram, L. N., Lee, H., & Ahn, S.-H. 2019, Nature Astronomy, 3, 766
- Hoang, T., Tram, L. N., Lee, H., Diep, P. N., & Ngoc, N. B. 2021, ApJ, 908, 218
- Indebetouw, R., de Messières, G. E., Madden, S., et al. 2009, ApJ, 694, 84
- Jekel, C. F., & Venter, G. 2019, pwlf: A Python Library for Fitting 1D Continuous Piecewise Linear Functions
- Jones, T. J., Bagley, M., Krejny, M., Andersson, B. G., & Bastien, P. 2015, AJ, 149, 31
- Jones, T. J., Klebe, D., & Dickey, J. M. 1992, ApJ, 389, 602
- Kataoka, A., Tsukagoshi, T., Pohl, A., et al. 2017, ApJL, 844, L5. doi:10.3847/2041-8213/aa7e33
- Lazarian, A. 2007, JQSRT, 106, 225
- Lazarian, A., & Hoang, T. 2007, MNRAS, 378, 910
- Lazarian, A. & Hoang, T. 2019, ApJ, 883, 122.
doi:10.3847/1538-4357/ab3d39
- Lazarian, A., Andersson, B.-G., & Hoang, T. 2015, Polarimetry of Stars and Planetary Systems, 81
- Lee, H., Hoang, T., Le, N., & Cho, J. 2020, ApJ, 896, 44
- Lee, M. Y., Madden, S. C., Le Petit, F., et al. 2019, A&A, 628, A113
- Lopez, L. A., Krumholz, M. R., Bolatto, A. D., Prochaska, J. X., & Ramirez-Ruiz, E. 2011, ApJ, 731, 91
- Mathis, J. S., Mezger, P. G., & Panagia, N. 1983, A&A, 500, 259
- Medan, I., & Andersson, B. G. 2019, ApJ, 873, 87
- Meixner, M., Panuzzo, P., Roman-Duval, J., et al. 2013, AJ, 146, 62
- Newville, M., Stensitzki, T., Allen, D. B., & Ingargiola, A. 2014, LMFIT: Non-Linear Least-Square Minimization and Curve-Fitting for Python, v.0.8.0, Zenodo, doi:10.5281/zenodo.11813
- Ngoc, N. B., Diep, P. N., Parsons, H., et al. 2021, ApJ, 908, 10
- Okada, Y., Güsten, R., Requena-Torres, M. A., et al. 2019, A&A, 621, A62
- Pattle, K., Lai, S.-P., Hasegawa, T., et al. 2019, ApJ, 880, 27
- Pattle, K., Lai, S.-P., Wright, M., et al. 2021, MNRAS, 503, 3414. doi:10.1093/mnras/stab608
- Pedregosa, F., Varoquaux, G., Gramfort, A., et al. 2011, Journal of Machine Learning Research, 12, 2825
- Pillai, T. G. S., Clemens, D. P., Reissl, S., et al. 2020, Nature Astronomy, 4, 1195
- Planck Collaboration, Aghanim, N., Akrami, Y., et al. 2020, A&A, 641, A12
- Reissl, S., Wolf, S., & Brauer, R. 2016, A&A, 593, A87
- Roman-Duval, J., Gordon, K. D., Meixner, M., et al. 2014, ApJ, 797, 86
- Santos, F. P., Chuss, D. T., Dowell, C. D., et al. 2019, ApJ, 882, 113
- Soam, A., Andersson, B. G., Acosta-Pulido, J., et al. 2021a, ApJ, 907, 93
- Soam, A., Andersson, B. G., Straižys, V., et al. 2021b, AJ, 161, 149
- Stephens, I. W., Yang, H., Li, Z.-Y., et al. 2017, ApJ, 851, 55. doi:10.3847/1538-4357/aa998b
- Tram, L. N., Hoang, T., Lee, H., et al. 2021a, ApJ, 906, 115
- Tram, L. N., Lee, H., Hoang, T., et al. 2021b, ApJ, 908, 159
- Vaillancourt, J. E., Andersson, B. G., Clemens, D. P., et al. 2020, ApJ, 905, 157
- Whittet, D. C. B., Hough, J. H., Lazarian, A., & Hoang, T. 2008, ApJ, 674, 304